studied for some time [2]. Recently, it was proven that the solution is unique and stable in computed tomography (CT) if a small region in the ROI is known *a priori* [3-8]. Inspired by these works, the first author has presented some work on interior problem in SPECT imaging [9-10]. Previous work was performed analytically. In this paper the SPECT interior reconstruction problem is solved using an iterative algorithm.

The paper is organized as follows: Section II shows the method we used to simulate the combined parallel-hole and pinhole collimated imager and the algorithm to reconstruct the pinhole data. The result of a numerical simulation is presented in Section III where comparisons are made to illustrate the quantitation improvement with the camera. Then the conclusion is given in Section IV.

II. METHODS

We performed a simulation using the digital XCAT brain phantom [11]. The phantom was stored in a 3-dimensional volume with each voxel being $(2mm)^3$. The center of the volume was assumed to be the origin of the global coordinate system. One slice of the phantom is shown in Fig. 2.

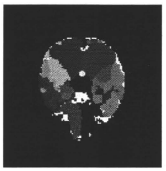

Fig. 2. The original XCAT phantom.

The large field of view parallel-hole collimated detector was simulated to revolve around the brain and acquire data every 5 degrees over half a circle. The detector bin was 0.28 cm along the transaxial direction and 0.2 cm along the axial direction. Poisson noise was manually added to the data to give a noise level such that the total counts of each slice summed to 10^7. The filtered backprojection algorithm was applied to the simulated projection data to reconstruct a volumetric image. Fig. 3 gives an example of one slice of the reconstructed low resolution volume. The image was interpolated and smoothed and was later used as the initial image and the prior information in the reconstruction of the pinhole data.

Fig. 3. The reconstructed image from parallel-hole projection data.

The pinhole collimator is shown in Fig. 4. It had a circular aperture with a radius of 0.5 mm and a knife edge with an opening angle of $\pi/3$. When the detector was localized close to the object, the projections were truncated as in Fig. 5. In the figure, the detector bin was 1.6 mm. The 2-dimensional detector plane had an area of 22.5×22.5 cm^2. In the simulation, pinhole collimated detector was assumed to be revolving to acquire 90 projections over a circle.

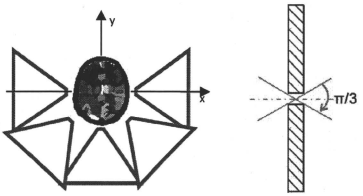

Fig. 4. The pinhole collimator. The pinhole is circular aperture with a radius of 0.5mm and a knife edge with an opening angle of $\pi/3$.

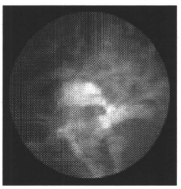

Fig. 5. Truncated projection data acquired by the pinhole collimated detector.

The reconstruction solved a linear system of equations $p=Af+noise$ for f which maximizes *a posteriori* probability $P(f|p)$. Since the *a posteriori* probability is

the product of the likelihood and the prior probability, the cost function can be expressed in two terms:

$$\Psi = -L(p \mid f) - \ln(\Phi(f)),$$

where the first term comes from the likelihood and the second term from the prior. Using the Gibbs prior

$$\Phi(f) = \frac{1}{Z} e^{-\beta U(f)},$$

the estimate was determined using the following procedure in a one-step-late algorithm [12]:

$$f_i^{new} = f_i^{old} \frac{\sum_j a_{ji} \frac{p_j}{\sum_{i'} a_{ji'} f_{i'}^{old}}}{\sum_j a_{ji} + \gamma^2 \frac{\partial}{\partial f_i} U(f^{old})}. \quad (1)$$

In this study, the energy term U(f) broke into two terms in the iteration step: one was a total variation penalty to account for the smoothness, the other included the prior information. Hence the procedure was

$$f_i^{new} = \frac{f_i^{old} \sum_j a_{ji} \frac{p_j}{\sum_{i'} a_{ji'} f_{i'}^{old}}}{\sum_j a_{ji} + \gamma_1^2 \frac{\partial}{\partial f_i} U_1(f^{old}) + \gamma_2^2 \frac{\partial}{\partial f_i} U_2(f^{old}, f_p)}$$

where γ_1 and γ_2 are regularization parameters. The first energy term U_1 utilized the total variation [13] of the reconstructed image. The second energy term was the distance between the estimate and the prior image f_p within the region of interest:

$$U_2(f^{old}, f_p) = \sqrt{\sum_{i \in ROI} (f^{old}(i) - f_p(i))^2}.$$

III. Results

In the simulation the pinhole data were acquired with truncation, resulting in reconstructing an interior problem. Efforts should be made to correct for the effect of this problem. Otherwise degradation is evident as shown in Fig. 6.

In this work, we used the low resolution image obtained by the large field of view detector first as the initial estimate in the iterative reconstruction of the pinhole data. Also, the low resolution image provided a priori information for the reconstruction of the interior problem.

The result is shown in Figs. 7 and 8. In this study, the L2 norm distance from the reconstructed image to the prior image was used in the penalty term. The image quality of the central part, which was the region of interest, was improved. The vertical and horizontal profiles crossing the center are shown in Fig. 8. From the profiles we see that the details of the image are more distinct by reconstructing both parallel-hole projection data and pinhole projection data; for instance, the details indicated by the arrows in Fig. 8.

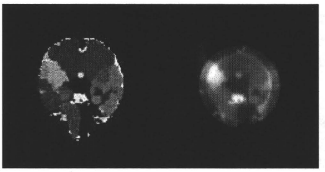

Fig. 6. Truncation effect. In both simulations, the pinhole collimated detector rotates around the object to acquire 90 views of projections and the same MAP estimate was performed with total variation regularization. The left image shows the result when there is no truncation and the right image shows the result with truncation. Degradation is evident in the right image due to the lack of correction for the interior reconstruction problem.

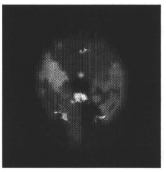

Fig. 7. Reconstructed image from pinhole data with interior problem and limited angular sampling. MAP estimate with regularization is applied.

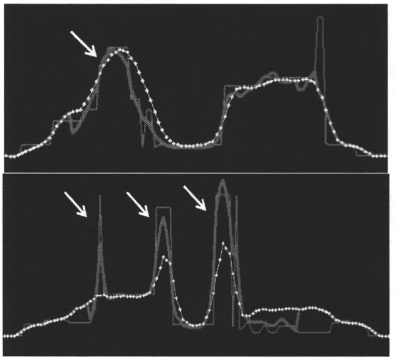

Fig. 8. Vertical and horizontal profiles crossing the center of the image. The purple solid line (thin) indicates the original phantom. The yellow dot-dash line is for the reconstructed image (Fig. 3.) from parallel-hole collimated data. While the red solid line (thick) is for the reconstructed image in Fig. 7.

IV. CONCLUSION

The combination of a large field of view parallel-hole collimated detector and smaller field of view high resolution pinhole detectors improves the quantitation in simulated brain imaging. It makes use of the high sensitivity of the pinhole collimator while compensates for the degradation in the reconstructed image due to the interior reconstruction problem caused by the small field of view of the pinhole collimator. This work will be verified through phantom imaging studies and patient imaging studies used to diagnose brain ischemia.

REFERENCES

[1] R. J. Jaszczak, J. Li, H. Wang, M. R. Zalutsky, and R. E. Coleman, "Pinhole collimation for ultra-high-resolution, small-field-of-view SPECT," *Phys. Med. Biol.*, vol. 39, pp. 425-437, 1994.

[2] F. Natterer, *The Mathematics of Computerized Tomography* (SIAM), 1986.

[3] G. Wang, Y. Ye and H. Yu, "General VOI/ROI reconstruction methods and systems using a truncated Hilbert transform," Patent disclosure submitted to Virginia Tech. Intellectual Properties on May 15 2007.

[4] Y. Ye, H. Yu, and G. Wang, "Exact interior reconstruction with cone-beam CT," *Int. J. Biomed. Imaging,* Article ID. 10693, 2007.

[5] Y. Ye, H. Yu, Y. We and G. Wang, "A general local reconstruction approach based on a truncated Hilbert transform," *Int. J. Biomed. Imaging*, Article ID. 63634, 2007.

[6] Y. Ye, H. Yu, and G. Wang, "Exact interior reconstruction from truncated limited-angle projection data," *Int. J. Biomed. Imaging*, Article ID. 427987, 2008.

[7] M. Courdurier, F. Noo, M. Defrise and H. Kudo, "Solving the interior problem of computed tomography using a priori knowledge," *Inverse Problems*, vol. 24, pp. 065001, 2008.

[8] H. Kudo, M. Courdurier, F. Noo, and M. Defrise, "Tiny a proiri knowledge solves the interior problem in computed tomography," *Phys. Med. Bio.*, vol. 53, pp. 2207-2231, 2008.

[9] Q. Huang and G. T. Gullberg, "Exact Reconstruction from Uniformly Attenuated Truncated SPECT Projection Data with Tiny a Priori Knowledge," IEEE Nuclear Science and Medical Imaging Conference, Oct 25-31, 2009, Orlando.

[10] Q. Huang, T. Zeniya, H. Kudo, H. Iida, G. T. Gullberg "Interior SPECT reconstruction problem with tiny a proiri knowledge – an application for high resolution pinhole brain imaging," Proceedings of Fully 3D Meeting and HPIR Workshop, Sep. 5-10, 2009, Beijing, China, pp. 358-361.

[11] W. P. Segars and B. M. W. Tsui, "MCAT to XCAT: the evaluation of 4-D computerized phantoms for imaging research," Proceedings of the IEEE, vol. 97, No. 12, 2009.

[12] P. J. Green, "Bayesian reconstructions from emission tomography data using a modified EM algorithm," *IEEE Transactions on Medical Imaging*, vol. 9, pp 84-93, 1990.

[13] V. Y. Panin, G. L. Zeng, and G. T. Gullberg, "Total variation regulated EM algorithm," IEEE Transactions on Nuclear Science, vol. 46, pp. 2202-2210, 1999.

A Monte Carlo estimation of effects of activity outside field of view in O-15 cardiac 3D-PET

Yoshiyuki Hirano, Kazuhiro Koshino and Hidehiro Iida, *Member IEEE*

***Abstract*– 3D-PET (Positron Emitter Tomography) is widely used for quantification of myocardial blood flow. Quantification of myocardial blood flow is very important for enhancement of the sensitivity and the specificity [1]. In the case of an O-15 cardiac PET, the heart is placed in the center of a field of view (FOV) and the liver which can be main background is placed outside FOV (OFOV). In a phase, the liver can have ~1.5 times larger activity than that of the heart. If large activity exists in OFOV like an O-15 cardiac PET, are scatter events corrected accurately? Is the quantification of myocardial blood flow assured? The purpose of this study is to figure out effects of OFOV activity on the quantification, and evaluate a scatter correction by using Monte Carlo simulation (Geant4) and fundamental phantom experiments. First, in order to validate the simulation, we made a comparison of a scatter fraction between simulations and experiments. The scatter fraction is measured according to NEMA-NU2007. We found out that, in the simulation, to construct structures like a bed and a front shield in OFOV is better to reproduce results of the experiment. Next, fundamental phantom experiments of 4 cases are performed. Case 1 has a decentering phantom placed in FOV. Case 2, 3, and 4 have an additional cylindrical phantom in OFOV, which has larger activity than the phantom placed in FOV by 1, 2, and 5 times. FOV phantoms have equivalent initial activity in all cases. Meanwhile, simulations are also performed with same configurations of these cases. Both the experiment and the simulation overestimate quantification of ROI (region of interest) values of FOV phantom in Case 2, 3 and 4. Finally, a realistic simulation using a numerical human model was performed aimed at an O-15 cardiac PET. We also obtained overestimations of ROI value in the heart due to the activity of the liver placed in OFOV. But quantifications of myocardial blood flows remained unchanged. Because myocardial blood flows are calculated from the clearance of O-15. When large activity exists in OFOV like the liver has, the scatter correction is insufficiency, which however dose not effects on the quantifications of myocardial blood flow in the O-15 cardiac PET.**

I. Introduction

3D-PET (Positron Emitter Tomography) is widely used for quantification of myocardial blood flow. In the case of O-15 cardiac PET, the liver is placed in OFOV. The liver can have ~1.5 times larger activity than that of the heart in a phase. If large activity exists in OFOV, are scatter events corrected accurately? The purpose of this study is to figure out effects of the activity in OFOV on the quantification, and evaluate a scatter correction by using of Monte Carlo simulation (Geant4) and fundamental phantom experiments. We performed three different simulations or experiments. First, in order to verify the adequacy of the simulation, we made a comparison of scatter fraction between a simulation and an experiment. In this simulation, structures in OFOV such as a front shield and a bed are included to simulate scatters originated from materials in OFOV. We also compared scatter fractions between a realistic configuration and a simple geometry, which include only a scintillator ring and a bed. Next, to investigate effects of OFOV activity on the quantification, fundamental phantom experiments (Case 1-4) with large activity in OFOV are conducted. Case 1 has one decentering phantom in FOV. Case 2-4 has an additional cylindrical phantom in OFOV. The OFOV phantom has larger activity than that of the FOV phantom by 1, 2, and 5 times. Simulations with same configuration of the phantom experiments are also performed. Finally, a realistic simulation using a numerical human model was performed aimed at an O-15 cardiac PET. Effects of the OFOV activity on myocardium blood flows are investigated by the simulation.

Y.Hirano, K. Koshino and H.Iida are with the Department of bio-medical imaging, The Advanced Medical Engineering Center, National Cerebral and Cardiovascular Center, 5-7-1 Fujishirodai, Suita City, Osaka, 565-8565 Japan (e-mail: hirano@ri.ncvc.go.jp).

II. Materials and Methods

The scatter fraction has measured with a PET (ECAT ACCEL) in 3D acquisition mode. The scintillator of the PET is LSO, which has intrinsic radioactivity. The measured scatter fraction thus is considered the radioactivity according to the NEMA-NU2007. We use scatter phantom for the measurement of the scatter fraction. The phantom is made of polyethylene with 700 mm length and 200 mm diameter. The tube with 700 mm length is filled with positron emitter (F-18), and inserted the scatter phantom at 45 mm apart from the center. In order to reduce effects of OFOV activity, we measured another scatter fraction, where we put activity in only FOV (FOV scatter fraction). Meanwhile, we calculated scatter fractions with a simulation, where structures are constructed as strict as possible. The front shield, the end shield, the septa, the supporting system of electric circuits, the rod sources, PMTs, the container of PMTs, room walls, ceiling, and floor are considered. In addition, a simulation with a simple geometry which has only the scintillator ring, the front shield, the end shield and the bed was performed. We made the comparison two different scatter fractions between the simulation (with the realistic geometry and with the simple geometry) and the experiment for the verification of this simulation.

Next, fundamental phantom experiments of 4 cases were performed to estimate effects of OFOV activity on the quantification. Case 1 has a decentering phantom with 200 mm diameter and 200 mm length in FOV. The phantom has

cold volume with 100 mm diameter and 200 mm length located at 50 mm shift from the center. The phantom is filled with 5 mCi (F-18) as initial activity. Case 2, 3, and 4 have additional cylindrical phantom in OFOV, and the phantom has the 1, 2, and 5 times larger activity than the FOV phantom. Initial activities of the FOV phantom in Case 2-4 are equivalent to the activity in Case 1. After the reconstruction of images by filtered back projection (FBP) with a scatter correction (SSS: single scatter correction), region of interest (ROI) values of the FOV phantom are calculated. If the scatters or randoms originated from OFOV activity are corrected accurately, same ROI values will be obtained in all cases. Meanwhile, the validated simulation was performed with strictly reproduced geometrical configuration of these cases, and created sinograms suitable for ECAT format. The images are reconstructed by a reconstruction method with a scatter correction (SSS) installed in the PET (ECAT ACCEL) system. Then we can obtain four types of image. One is an image reconstructed with the scatter correction and without the scatter correction. The other one is an image using only scatter events (scatter image). The last one is an image using non-scatter events (true image). In actual examinations, we never obtain a scatter image and a true image. If scatters are corrected accurately, a scatter corrected image is almost same as a true image. We put ROI on the FOV phantom and compared ROI values among 4 cases.

Finally, the simulation with realistic geometry using a numerical human model was performed. The model is developed by National Institute of Information and Communications [2] in Japan, which is consist of ~5 million voxels with 2 mm cubic, and based on MRI images of average Japanese of male and female shown in Fig.1. We can discriminate 51 organs or tissues and ID numbers are assigned to each voxel. We gave attenuation coefficients obtained from the MIRD (Medical Internal Radiation Dose) to these organs or tissues. We calculated attenuation map analytically. In this simulation, we gave activity to the heart, the liver, and the lung along to the organ activity derived from a clinical examination shown in Fig. 2. Sinograms are created and images are reconstructed for each phase. The differences between ROI values in scatter corrected image and the true image are investigated. The differences indicate the insufficiency of the scatter correction. We created two different input functions and tissue curves using scatter corrected images and true images, and myocardial blood flows are calculated with one compartment model in both curves.

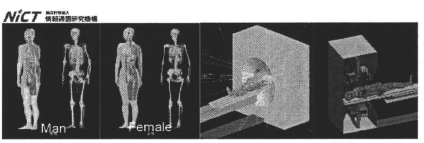

Fig.1 Left two figures show Numerical human modes developed by National Institute of Information and Communications in Japan. Right two figures show the Geant4 simulation with the numerical human model.

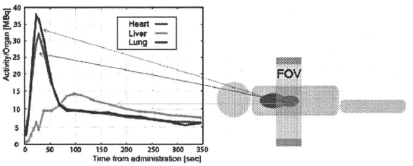

Fig.2 Time activity curves of the heart, the liver, and the lung derived from an O-15 cardiac PET examination. These curves are obtained by PET images (Bq/cc) and organ volume of the numerical human model.

III. RESULT

Average scatter fractions of all slices (1-175) are 45.0 % with the experiments, 45.9 % with the simulation using the realistic geometry, and 45.2 % using the simple geometry. Average FOV scatter fractions (activity exists in FOV) of the experiment, the simulation with the realistic geometry, and with the simple geometry are 37.8 %, 36.3 %, and 33.0 %, respectively. Axial distributions of the scatter fraction and the FOV scatter fraction are shown in Fig 3 (left) and Fig. 3 (right), respectively. The simulation with the realistic geometry has consistent with that of the experiment in both scatter fractions. On the other hand, though the simulation with the simple geometry reproduced the average scatter fraction, the axial distribution has difference especially that of FOV scatter fraction. From the results of the simulation, materials which contribute scatter are listed in Table 1. The scatter phantom predictably has main contribution to scatters. About eighty-nigh percent of total scatter events are scattered by the phantom including the source tube. The second contribution material is the bed, which has 3 % of total scatters.

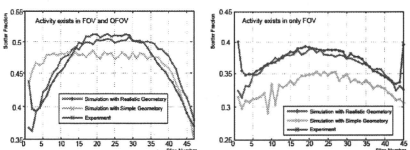

Fig. 3 The axial distribution of scatter fraction and FOV scatter fraction. The blue line shows the experiment. The red line shows the simulation with the realistic geometry, and the green line shows the simulation with simple geometry. Both in two different scatter fraction, the simulations with realistic geometry are closer to the experiment than the simple geometry.

Table 1 Scatter materials derived from the simulation. About 89 % of scatter event is scattered by the scatter phantom. Structures in OFOV have small contribution to the scatter.

Material	% of total scatter
Scatter Phantom	85.9 %
Source tube	2.9 %
Bed	2.9 %
PMT Container	2.7 %
Rod source support system	2.0 %
Gantory	2.0 %
Septa	0.43 %
Front Shield	0.44 %
Air	0.28 %

The reconstructed phantom images of the experiment with the scatter correction and without the scatter correction are shown in Fig.4 (left) together with a circular ROI. The simulation images of four types of images (with the scatter correction, without the scatter correction, the true image, and the scatter image) are shown in Fig.4 (right). ROI values normalized by that of case 1 are listed in Table 2. Because FOV phantoms have same initial activity in all cases, the ROI values of all cases should be equivalent. However, Case 2, 3 and 4 overestimated by ~3 %, ~9 %, and ~15 %, respectively in both the simulation and the experiment.

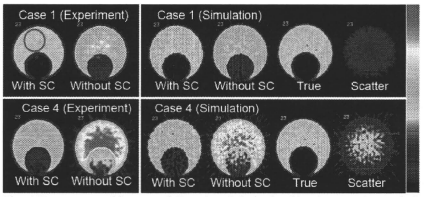

Fig. 4 Reconstructed images of Case 1 and 4 obtained by the experiment (left tow figures) and the simulation (right tow figures). A circular ROI is drawn in scatter corrected image of Case 1 (experiment). The comparison of ROI values in all cases are listed in table 2.

Table 2 ROI values normalized by that of Case 1. Because initial activity of each case was set to same activity, 5mCi, ROI values should be equivalent. However, in the case of activity exists in OFOV, overestimation was obtained in Case 2, 3, and 4.

	Case 1	Case 2	Case 3	Case 4
Experiment	1	1.03	1.09	1.15
Simulation	1	1.02	1.04	1.13

Activities of the heart, the liver and the lung derived from a clinical cardiac O-15 PET are shown in Fig.2. In the examination, part of the liver and the lung are imaged and the activity is obtained by an unit Bq/cc. We thus calculated activity of the whole organ by Bq/cc × volume calculated using the numerical human model. The simulation images of 20, 45, 75, 120, 210, 300 sec from administration are shown in Fig. 5. An example of ROI in the apex is shown in the image of 20 sec. In some phases, scatter corrected images overestimated true images. Input functions and tissue time activity curves derived from the scatter corrected images and the true images are shown in Fig. 6. Finally, myocardial blood flows calculated though one compartment model using these input functions and tissue curves are listed in Table 3. Myocardial blood flows of apex, anterior, lateral, posterior, and septal remained unchanged.

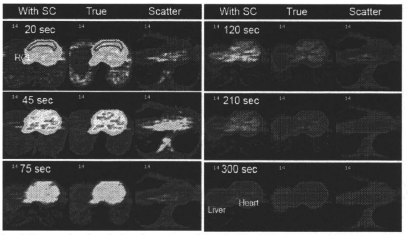

Fig. 5 Dynamic simulation images at 20, 45, 75, 120, 210, and 300 sec. Time span after ~75 sec from administration is washout phase. In the washout phase, almost same scatter images were obtained, which indicates scatters do not change washout rate.

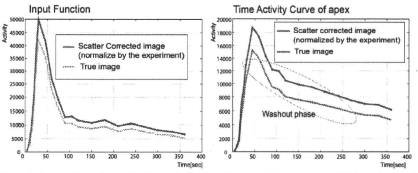

Fig. 6 Input functions (left) and tissue time activity curves (right) derived from scatter corrected images and true images. These curves of scatter corrected images are normalized by these of the experiment.

Table 3 Myocardial blood flows (mL/min/g) calculated using scatter corrected images and true images. Even in the case of using true images, myocardial blood flows did not change.

MBF (mL/min/g)	With SC image	True image
Apex	1.09	1.11
Anterior	0.81	0.80
Lateral	1.03	1.03
Posterior	0.80	0.79
Septal	0.75	0.73

IV. Discussion

The simulation, especially with realistic geometry, has good agreement with the experiment in scatter fractions and the distribution. This simulation can be a useful tool for estimating scatter. Meanwhile, simulation with the simple geometry underestimated of the FOV scatter fraction. This indicates that materials outside FOV slightly increase scatter. It is better to construct structures outside FOV for accurate simulation. However contribution of the materials to scatter is several percent. If we do not need high accuracy, these structures should not be considered to reduce the calculating time.

From the results of the phantom experiments and the simulation, in the case of large activity exists in OFOV, the scatters are not corrected accurately, which causes overestimated ROI values. However, even in an extreme case

(Case 4), the overestimation is ~15 %. In the simulation, we also obtained good agreements with the experiment.

In a clinical O-15 cardiac PET, the liver has ~1.5 time larger activity than that of the heart at 100 sec from administration. This case is similar to the Case 3 of phantom experiment. The scatters are not compensated accurately same as Case 3. Consequently, ROI values tend to overestimate true values. This result indicates that some quantitative physiological parameters measured by PET may be overestimated. However, physiological parameters do not always depend on absolute ROI values. Quantitative myocardial blood flows determined by O-15 seem to epitomize this case. Because the blood flows are calculated by the tissue washout rate, which is equivalent both in scatter corrected images and true images. As shown in Fig. 5, uncorrected scatters make a constant contribution to the ROI values in the heart region at the washout phase, and this leaves myocardial blood flow unchanged.

V. Conclusions

Our simulation using Geant4 has good agreements with experiments in scatter fractions and the phantom experiments. It is preferable to construct structures outside FOV for accurate simulation. A bed and containers of PMTs and scintillator have several percent contributions to increase of scatter.

Scatters originated from activity outside FOV are not compensated accurately. Larger activity outside FOV, larger overestimation is observed.

In the simulation of O-15 cardiac PET, due to the large activity of the liver, overestimated ROI values in the heart were obtained. However the overestimations do not matter for quantifications of myocardial blood flows.

References

[1] J. Kunuti, S. Kajander, M Maki & H. Ukkonen, "Quantification of myocardial blood flow will reform the detection of CAD", *Journal of Nuclear Cardiology*, Vol.16, No.4, pp.497-506, 2009

[2] Nagaoka T, Watanabe S, Sakurai K, Kunieda E, Watanabe S, Taki M, & Yamanaka Y. "Development of Realistic High-Resolution Whole-Body Voxel Models of Japanese Adult Male and Female of Average Height and Weight, and Application of Models to Radio-Frequency Electromagnetic-Field Dosmietry". *Physics in Medicine and Biology*, Vol,49, No.49, pp1-15, 2004

Development of a high resolution and quantitative SPECT for the human brain

Y. Hirano, T. Zeniya, and H. Iida, *Member, IEEE*

Abstract– **We are developing a high resolution and quantitative SPECT for the human brain. The SPECT has two types of detector, a large FOV detector with a parallel collimator and a small FOV detector with a pinhole collimator. A quantitative and high resolution image is reconstructed by the small FOV detector using a supporting image obtained by the large FOV detector. The large FOV detector consists of a NaI(Tl) scintillator (147 × 250 × 6.4 mm^3) and 15 flat panel type multi-anode PMTs (H8500, Hamamatsu) arranged on 5×3 matrix. H8500 has 8×8 anodes with 5.8 mm^2. We have constructed the large FOV detector and checked the performance. We also took SPECT images of a cylindrical phantom, a 3D brain phantom and multi line sources. An interaction point is calculated by the Anger method using all anodes (40×24). The observed intrinsic spatial resolution (FWHM mm) in *x* and *y*-direction were 3.5 mm and 3.1 mm, respectively. But these are less than we expected. We aimed at ~2 mm, which is better resolution than clinical SPECTs ~4, 5 mm. To improve the spatial resolution, we proposed a method instead of the Anger method and estimated the performance by using of a Monte Carlo simulation of scintillation lights (Geant4). To identify an interaction point, reference data set of distribution of scintillation lights on the PMT anodes is used. The reference data set is previously measured at known incident positions. For each event, the most similar distribution with the reference data set determined by a least squared method is identified as the interaction point. Using the method, 1.8 mm resolution is expected.**

Meanwhile, the small FOV detector is under the construction. We use a $LaBr_3$(Ce) scintillator (100 × 100 × 4 mm^3) and 4 H8500s. We measured the physical performance, spatial and energy resolution and the position dependence. The intrinsic spatial resolution in *x* and *y*-direction and the energy resolution are 2.3 mm, 2.4 mm and 6.1 %, respectively.

I. Introduction

We are developing a high resolution and quantitative Single Photon Emission Computed Tomography (SPECT) for the human brain. This SPECT has two types of detector. One is a large field of view (FOV) detector and the other is a small FOV detector. The large FOV detector views the whole human brain with a parallel collimator. The small FOV detector views localized region with pinhole or cone-beam collimators. In the case of a larger subject than a FOV like the human brain, the projection data are truncated by radioisotope outside of a small FOV. Due to the truncation, on the reconstructed image, the artifact appears and the voxel values are overestimated. This hampers quantitative assessment of physiological functions. We have developed a new truncation compensated 3D-OSEM (TC-3DOSEM) reconstruction method. We use an image of the large FOV detector without truncation as an initial image of the reconstruction by the small FOV detector. The truncated data can be successfully reconstructed [1] [2]. The conceptual diagram and aspect of the detector are shown in Fig.1. The large FOV detector has been completed, and checked the performance. The observed intrinsic spatial resolution in *x* and *y*-direction were 3.5 mm and 3.1 mm, respectively. Some phantom images were taken by the large FOV detector. The obtained spatial resolution from the SPECT image is ~3.3 mm (FWHM), which is comparable with the intrinsic resolution. However we expect the better resolution ~2 mm. Then, we proposed other method and estimated the performance by a Monte Carlo simulation of scintillation lights (Geant4).

Meanwhile, the small FOV detector is under the construction. The small FOV detector is consist of $LaBr_3$(Ce) scintillator (100×100×4 mm^3) and the 4 H8500 PMTs. We measured the intrinsic spatial and energy resolution.

Objectives of this work are twofold. The one is to estimate proposed method for better spatial resolution of the large FOV detector by a simulation, and to verify the adequacy of the simulation. The other is to evaluate performance of the small FOV detector.

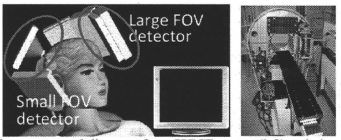

Fig.1 The conspectrual diagram of our SPECT system (left) and picture of a pilot unit (right).

II. Materials and Methods

The large FOV detector has constructed. The detector consist of NaI(Tl) scintillator (147×250×6.4 mm^3), 15 flat panel type multianode H8500 PMTs (Hamamatsu). The PMT has 64 small anodes (5.2×5.2 mm^2). The PMTs arranged in 5×3 matrix are coupled to the scintillator by optical grease (BC630). The scintillator is covered with a white diffuse reflector except for connection side of PMTs. An interaction point is calculated by the Anger method using all anodes arranged in 40×24 matrix. The intrinsic spatial resolution and energy resolution were measured using a special designed collimator made of lead with 10 mm thickness. The collimator has 170 holes with 1.5 mm diameter located on 17×10 grid pattern. The grid interval is 15 mm. The collimator is put on the scintillator, and point sources of Tc-99m (141keV) are

Y.Hirano, T. Zeniya and H.Iida are with the Department of bio-medical imaging, The Advanced Medical Engineering Center, National Cerebral and Cardiovascular Research Center Institute, 5-7-1 Fujishiro-dai, Suita City, Osaka, 565-8565 Japan (e-mail: hirano@ri.ncvc.go.jp).

placed at each hole. Resolutions at each grid point are measured using the collimator and the average experimental resolutions were calculated [3]. The results of experimental resolutions are used for a validation study of a Monte Carlo simulation. Meanwhile, we took images of some phantoms by the large FOV detector attached with a parallel collimator. A 3D brain phantom, a cylindrical phantom with 200 mm length and 180 mm diameter, and multi line sources were imaged. Image spatial resolution is calculated using an image of multi line sources. The reconstruction method is OESM with an absorption correction, a scatter correction and a resolution recovery.

We simulated the scintillation lights to estimate resolutions with geometrical configuration shown in Fig 2. The configuration includes the scintillator, reflector, optical window, optical grease, PMT windows, and PMT anodes. The simulated processes are described in followings. (1) Gamma rays enter the scintillator at 170 holes vertically. (2) Scintillation lights radiate at an interaction point. (NaI(Tl): 38000 photons/MeV) (3)Scintillation lights propagate though the scintillator, optical window, and PMT window. Both optical and PMT window are made of bolosilicate glass. (4) Optical processes, reflection, refraction at boundaries and absorption are included. (5)When scintillation lights reach an anode, detection or not are determined by the quantum efficiency and the collection efficiency (60 %) of H8500. An interaction point is calculated by the Anger method. Optical properties such as transparency and refractive indexes are considered. Some of them have wavelength dependence. We assembled material optical properties from brochures of products.

To verify the adequacy of the simulation, spatial and energy resolution were compared with experimental resolutions. 3000 gamma-ray beams enter the scintillator above each hole.

In order to improve the spatial resolution of the large FOV detector, another method of identification of interaction points was tried. In this method, reference data set of distributions of scintillation lights on the PMT anodes are used for the identifications. Previously, a photon distribution is simulated at known interaction point. In this work, distributions were simulated at 1 mm grid pattern, and the total number of distributions is 37296 (252×148). The each reference distribution derived from the average of 100 distributions. Then, an interaction point is determined by comparison with the reference data set. The least square method is used for the determination. Interaction points in the validation study were recalculated using this method instead of the Anger method.

The small FOV detector has constructed. $LaBr_3(Ce)$ is employed as the scintillator for the better resolutions. The $LaBr_3(Ce)$ is $100 \times 100 \times 4$ mm^3 and 4 H8500s are used for the detection of the scintillation phantons. The intrinsic spatial resolution and energy resolution were measured same as the large FOV detector.

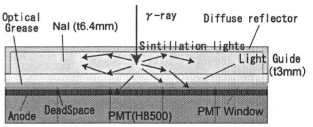

Fig.2 The simulation geometry of the large FOV detector. The scintillation lights propagates through the scintillator, optical window, optical grease and PMT windows until reaching PMT anodes. At the boundary of the reflector, the Lambert reflection is applied. At the other boundaries, Fresnel reflection and refraction are applied

III. Result

A planer image of 170 point sources by the large FOV detector is show in Fig. 3 (left). The observed intrinsic spatial resolution (FWHM) in x and y-direction were 3.5 mm and 3.1 mm, respectively. The energy resolution was 10 %. Meanwhile, the spatial resolution of the simulation in x and y-direction, and energy resolution were 3.3 mm and 3.0 mm, and 9 %, respectively. A planer image and energy spectra of center of the detector are shown in Fig. 3 (right) and Fig. 4.

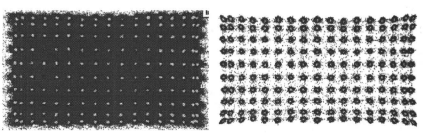

Fig. 3 Planer image of 170 points source by the large FOV detector obtained by the experiment (left) and the simulation (right). Spatial resolutions of the experiment and the simulation are 3.5 mm and 3.3 mm in x-direction, 3.3 mm and 3.0 mm in y-direction, respectively.

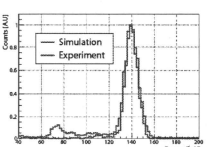

Fig. 4 Energy spectra of the center of the detector obtained by the experiment (red line) and the simulation (blue line). In the simulation, the broad of a peak is originated from fluctuation of the number of obtained scintillation photons. The energy resolution of the experiment and the simulation is 10 % and 9 %, respectively.

The reconstructed image of a 3D brain phantom, a cylindrical phantom and multi-line sources are shown in Fig. 7. The spatial resolution of image derived from the image of multi-line sources was ~3.3 mm.

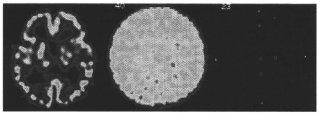

Fig. 5 Reconstructed images of a 3D brain phantom (left), a cylindrical phantom (center), and multi-line sources (right). The image spatial resolution is ~3.3 mm obtained from the multi-line sources.

With regard to the simulation study of the proposed identification method of interaction points, two examples of the reference data set of photon distribution and a planer image using the proposed method are shown in Fig. 6. The spatial resolution of x and y-direction are 1.8 mm and 1.8 mm, respectively.

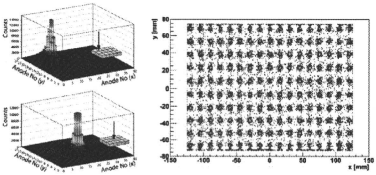

Fig. 6 Results of the proposed method by the simulation. Left two figures shows the example of the reference data of 100 gamma-rays average enter at the edge (upper left) at the center (under left). A planer image of 170 point sources is shown in the right. The spatial resolution of x and y direction was 1.8 mm and 1.8 mm, respectively.

Finally, intrinsic spatial resolution and energy resolution of the small FOV detector are 2.3 mm and 2.5 mm and 6.1 %, respectively. A planer image and an energy spectrum of the center of the detector are shown in Fig. 7.

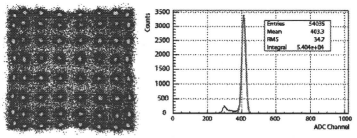

Fig.7 A planer image of 64 point sources by the small FOV detector (left). An energy spectrum of the center of the detector is shown in the right. The energy resolution is 6.1 % derived from a fitting of Gauss function.

IV DISCUSSION

The large FOV detector has 3.5 mm and 3.3 mm intrinsic spatial resolution in x and y-direction, respectively. We obtain comparable resolution in SPECT image derived from an image of multi-line sources. However, we aimed at ~2 mm resolution to differentiate clinical SPECTs, which have ~4 mm resolution. It seems to be that the worse resolution rather than expected is due to the larger error propagation of anode outputs. In the case of the Anger method, to increase photosensor does not have much contribution to enhancement spatial resolution. Conversely, large propagation of errors of photo-sensors may deteriorate the resolution. Therefore, we need to employ other method instead of the Anger method for better resolution in the large FOV detector.

The spatial resolutions of the simulation are consistent with those of the experiment within 10%. The accuracy seems to be sufficient to estimate resolutions and design new detectors. The simulation also has good agreement with experimental energy resolution. The energy spectrum is formed from the quantity of obtained photons. The energy resolution of simulations is usually generated using an adjustment parameter decided by an experiment. In this work, however, the energy resolution is calculated without such a parameter, depending on the number of photons.

The simulation results are always overestimated. Our simulation still does not consider other uncertainties, e.g., fluctuation of the number of electrons in the multiplying process of a PMT, etc. In addition, there are unknown optical properties such as the absorption length of the optical grease (in this study, however, the absorption can be treated as negligible because the grease layer is thin) and almost the properties does not have wavelength dependence. We need a dataset of optical properties of materials, especially those used in scintillation detectors. In order to conduct accurate simulations, it seems better to consider other uncertainties as much as possible. Although this simulation already has sufficient reproducibility, some optical properties are neglected.

The proposed method indicated improvement of spatial resolution from 3.5 mm to 1.8 mm in the x direction. The large FOV detector has the potential for high resolution, ~2 mm. One advantage of this method is that the unit of the planar image is actual length (mm); this is different from the Anger method, in which the unit is arbitrary. We do not need to calibrate position.

To implement this method, it is essential to install an analog to digital converter (ADC) for each anode. This conversion may take a great deal of time to convert and decrease the cost-effectiveness. However, it is worthwhile to try this method, because once all anode outputs are converted, we can try other methods. A neural network would be one promising method; another would be to employ a modified Anger method using restricted anodes that are peripheral to the largest output anode. We are developing a full digital system for the method. Furthermore, if the reference data is compiled using only simulations with high accuracy, the technique has the potential to discriminate the depth of interactions. It sometimes happens that a gamma ray is scattered before absorbed in the scintillator. In this case, there are multiple sources of scintillation lights, and these events impair spatial resolution. It is difficult to discriminate events with multiple scintillation sources from events with single scintillation source. Chi-square, defined by

$$\chi^2 = \frac{1}{ndf}\sum_i \frac{(obj_i - ref_i)^2}{error_i^2},$$

may help to make the distinction; here, i, obj, ref, $error$ ndf mean index of anode, anode output, anode output of reference data, error of anode output, and number of degrees of freedom, respectively. A large chi-square indicates an event with multiple scintillation sources. Higher-energy gamma rays, such as 511 keV, tend to be such an event. In a SPECT system, however, because of the low energy of gamma-rays (in the

range of several hundred keV), these occurrences are rare, and can safely be ignored.

With regard to the small FOV detector, better intrinsic spatial resolution 2.3 mm and 2.4 mm in x and y direction, respectively, were obtained, and these are comparable because the number of the anodes is same in x and y direction. However, ~2.3 mm resolution is worse resolution rather than expected resolution ~1.5 mm which is obtained by a simulation. Moreover, 1.1 mm spatial resolution with $LaBr_3$(Ce) scintillator was observed by Pani *et al* [4]. The detector is similar to the small FOV detector except for the size. The size of the scintillator is $50 \times 50 \times 4$ mm^3 with 3 mm thickness of optical window and covered with diffuse white reflector. One H8500 is attached by optical grease. We also simulate spatial resolution with this configuration, 0.94 mm resolution, which is comparable the experimental value was obtained. The simulation results would be reliable. We thus expect better resolution with the small FOV detector and the cause of the poor resolution is under the investigation. Meanwhile, a good energy resolution 6.1 % was observed.

CONCLUSION

We are developing a high resolution and quantification SPECT system for the human brain. SPECT imaging with the large FOV detector have done with ~3.3 mm spatial resolution. We proposed other method to improve the resolution instead of the Anger method and estimated the performance by a validated simulation. The simulation can reproduced special resolution of the large FOV detector within ~10 %. The results of the simulation indicated that the proposed method can improve the spatial resolution from ~3.3 mm to ~1.8 mm.

The small FOV detector has completed. The detector has ~2.5 mm spatial resolution and 6.1 % energy resolution, respectively.

REFERENCES

[1] T.Zeniya, H. Watabe, H. Kudo, Y. Hirano, K. Minata, and H. Iida, "Combination of a high resolution detector with small FOV and a low resolution detector with large FOV for high resolution and quantitative SPECT", *Nuclear Science Symposium and Medical Imaging Conference 2008, IEEE Conference Record*, pp. 5229-5231, 2008

[2] T. Zeniya, Y. Hirano, T. Sakimoto, K. Ishida, H. Watabe, N. Teramoto, H. Kudo, K. Minato, J. Hatazawa and H. Iida, "Conceptual Design of High Resolution and Quantitative SPECT system for Imaging a Selected Small ROI of Human Brain", *Nuclear Science Symposium and Medical Imaging Conference 2009, IEEE Conference Record*, pp.3484-3486, 2009

[3] Y.Hirano, T.Zeniya, H. Watabe, and H. Iida, "Performance Estimation of High Resolution SPECT for the Human Brain by Monte Carlo Simulation of Scintillation Lights", *Nuclear Science Symposium and Medical Imaging Conference 2009, IEEE Conference Record*, pp.3602-3605, 2009

[4] R.Pani, R. Pellegrinia, *et al*, "$LaBr_3$:Ce crystal: The latest advance for scintillation cameras", *Nuclear Instruments and Methods in Physics Research A*, vol. 572, pp.268–269, 2007

Eur J Nucl Med Mol Imaging (2010) 37:377–385
DOI 10.1007/s00259-009-1262-2

ORIGINAL ARTICLE

Quantification of regional myocardial oxygen metabolism in normal pigs using positron emission tomography with injectable ^{15}O-O_2

Takashi Temma · Hidehiro Iida · Takuya Hayashi · Noboru Teramoto · Youichiro Ohta · Nobuyuki Kudomi · Hiroshi Watabe · Hideo Saji · Yasuhiro Magata

Received: 27 April 2009 / Accepted: 10 August 2009 / Published online: 4 September 2009

Abstract
Purpose Although ^{15}O-O_2 gas inhalation can provide a reliable and accurate myocardial metabolic rate for oxygen by PET, the spillover from gas volume in the lung distorts the images. Recently, we developed an injectable method in which blood takes up ^{15}O-O_2 from an artificial lung, and this made it possible to estimate oxygen metabolism without the inhalation protocol. In the present study, we evaluated the effectiveness of the injectable ^{15}O-O_2 system in porcine hearts.
Methods PET scans were performed after bolus injection and continuous infusion of injectable ^{15}O-O_2 via a shunt between the femoral artery and the vein in normal pigs. The injection method was compared to the inhalation method. The oxygen extraction fraction (OEF) in the lateral walls of the heart was calculated by a compartmental model in view of the spillover and partial volume effect.
Results A significant decrease of lung radioactivity in PET images was observed compared to the continuous inhalation of ^{15}O-O_2 gas. Furthermore, the injectable ^{15}O-O_2 system provides a measurement of OEF in lateral walls of the heart that is similar to the continuous-inhalation method (0.71 ± 0.036 and 0.72 ± 0.020 for the bolus-injection and continuous-infusion methods, respectively).
Conclusion These results indicate that injectable ^{15}O-O_2 has the potential to evaluate myocardial oxygen metabolism.

Keywords Myocardial oxygen metabolism · PET · Pig · OEF · Injectable ^{15}O-O_2

T. Temma · H. Saji
Department of Patho-Functional Bioanalysis,
Graduate School of Pharmaceutical Sciences, Kyoto University,
Kyoto, Japan

H. Iida · T. Hayashi · N. Teramoto · Y. Ohta · N. Kudomi · H. Watabe
Department of Investigative Radiology,
National Cardiovascular Center Research Institute,
Osaka, Japan

Y. Magata (✉)
Laboratory of Genome Bio-Photonics,
Photon Medical Research Center,
Hamamatsu University School of Medicine,
1-20-1 Handayama,
Hamamatsu 431-3192, Japan
e-mail: magata@hama-med.ac.jp

Introduction

In the myocardium, fatty acid or glucose is used to produce energy by aerobic metabolism. Oxygen is one of the most important substrates closely related to the aerobic metabolism in the TCA cycle; thus, oxygen metabolism should be a direct reflection of myocardial metabolism of these substrates. Therefore, there has been considerable interest in the development of a method to quantify oxygen metabolism in the myocardium.

Recently, ^{11}C-acetate has been used for this purpose [1–5]. ^{11}C-acetate is taken up by the mitochondria and metabolically converted into acetyl-CoA. It then enters the TCA cycle and is transformed to ^{11}C-CO_2, which is cleared rapidly from the myocardium. Thus, the clearance pharmacokinetics reflects oxygen metabolism in the myocardium. However, the quantification of oxygen metabolism using ^{11}C-acetate is quite difficult because of various intermediary compounds.

The use of ^{15}O-O_2 gas inhalation and PET scanning can provide a quantitative myocardial metabolic rate for oxygen ($MMRO_2$) [6, 7]. The tracer kinetic model used is based on that originally proposed to describe the behavior of ^{15}O-O_2 in brain tissue [8, 9]. However, the direct translation of the

compartmental model for the brain to the heart is not permitted, because subtraction for spillover from gas volume in addition to that from the blood pool is needed. A previous study demonstrated that the gas volume can be accurately estimated from the transmission scan data; thus, this technique did not require additional emission scanning for estimating the quantitative gas volume images [6, 7]. However, gaseous radioactivity in the lung during the inhalation of ^{15}O-O_2 gas is too high in comparison to other regions. Subtraction for this contribution is straightforward and accurate using the transmission scan-derived gaseous volume images, but the lung radioactivity degraded image quality in the estimated $MMRO_2$ images.

As an alternative to gas inhalation, we recently developed a method to prepare an injectable form of ^{15}O-O_2. This was accomplished by exposing pre-collected blood to ^{15}O-O_2 gas using a small artificial lung system resulting in a maximum yield of 130 MBq/ml. We demonstrated that cerebral oxygen metabolism could be estimated in normal and ischemic rats using injectable ^{15}O-O_2 [10–12]. This technique has the potential of avoiding the inhalation protocol.

The aim of the present study was therefore to test the feasibility of using the injectable ^{15}O-O_2 oxygen system for estimating myocardial oxygen metabolism in pigs. The injection method was compared to the inhalation method to determine if the injection method resulted in a reduction of lung radioactivity, an improved image quality, a more accurate estimate of myocardial oxygen metabolism, and an improved signal-to-noise ratio.

Materials and methods

Theory

^{15}O-Oxygen was administered by IV injection or inhalation and was carried as ^{15}O-hemoglobin by blood to peripheral tissues including the myocardium, where it was converted to ^{15}O-water (^{15}O-H_2O_{met}) through aerobic metabolism. The increased distribution volume of ^{15}O-H_2O_{met}, represented by the exchangeable water space of tissue, causes delayed removal of radioactivity. This allows the definition of an appropriate model and equations to be derived for the calculation of a regional myocardial metabolic rate for oxygen ($rMMOR_2$) and regional oxygen extraction fraction (rOEF). Previous studies demonstrated that these calculations were similar to those used for estimating cerebral blood flow and oxygen metabolism and require the measurement of regional myocardial blood flow (rMBF) and a correction for spillover of activity from the vascular pools and the pulmonary alveoli [6, 7]. rMBF was measured by the ^{15}O-H_2O injection technique [13]. Activity in the vascular pools of the heart chambers and the lung was evaluated with a conventional measurement of blood volume using ^{15}O-CO, and activity in the pulmonary alveoli was evaluated with an unconventional and indirect measurement of gas volume obtained from the transmission scan. Furthermore, the existence of recirculating ^{15}O-H_2O_{met} in the blood freely accessible to the myocardium was taken into consideration.

The differential equation describing the myocardial kinetics after administration of ^{15}O-O_2 can be written as follows:

$$\frac{dC^{myo}(t)}{dt} = OEF \cdot f \cdot A_o(t) + f \cdot A_w(t) - \left(\frac{f}{p} + \lambda\right) C^{myo}(t) \quad (1)$$

where $C^{myo}(t)$ designates the true radioactivity concentration in the myocardium at time t, f is myocardial blood flow, $A_O(t)$ is the ^{15}O-O_2 radioactivity concentration in arterial blood, $A_W(t)$ is the ^{15}O-H_2O radioactivity concentration in arterial blood, p is the myocardium/blood partition coefficient of water, and λ is the physical decay constant of O-15.

Solving Eq. (1) in terms of $C^{myo}(t)$ gives:

$$C^{myo}(t) = OEF \cdot f \cdot A_o(t) * e^{-\left(\frac{f}{p}+\lambda\right)\cdot t} + f \cdot A_w(t) * e^{-\left(\frac{f}{p}+\lambda\right)\cdot t} \quad (2)$$

where the asterisk denotes the convolution integral. During steady-state conditions under the continuous administration of ^{15}O-O_2, the following relationship holds:

$$C^{myo} = \frac{OEF \cdot f \cdot A_o + f \cdot A_w}{\left(\frac{f}{p} + \lambda\right)} \quad (3)$$

In the actual PET studies, the spillover from vascular pools and pulmonary alveoli and the partial volume effect should be taken into consideration [14]. Then, the measured radioactivity concentration in the region of interest (ROI) in the myocardium ($R^{myo}(t)$) can be expressed as:

$$\begin{aligned} R^{myo}(t) = {} & \alpha \cdot C^{myo}(t) \\ & + (V_B^{myo} \cdot A_t(t) - \alpha \cdot F_{Vein} \cdot OEF \cdot A_o(t) - \alpha \cdot F_{Vein} \cdot A_w(t)) \\ & + V_G^{myo} \cdot C_{gas}(t) \end{aligned} \quad (4)$$

where α denotes the myocardial tissue fraction, V_B^{myo} is the myocardial blood volume, $A_t(t)$ is the total O-15 radioactivity concentration in arterial blood, F_{vein} is the microscopic venous blood volume, V_G^{myo} is the gas volume in the myocardial ROI and $C_{gas}(t)$ is the O-15 radioactivity concentration in V_G^{myo}.

With the bolus injection or infusion methods using an artificial lung system, the radioactivity in the pulmonary alveoli is expected to be negligible in comparison with the inhalation method. Thus, Eq. (4) can be converted to:

$$R^{myo}(t) = \alpha \cdot C^{myo}(t) + (V_B^{myo} \cdot A_t(t) - \alpha \cdot F_{Vein} \cdot OEF \cdot A_o(t) - \alpha \cdot F_{Vein} \cdot A_w(t)) \quad (5)$$

Subjects

In this study, four healthy miniature pigs (22–30 kg) were used. The pigs were anesthetized by IM injection of ketamine and xylazine followed by continuous infusion of propofol (5 mg/kg/h). The animals were then placed in the supine position on the bed of the PET scanner. All experimental procedures were approved by the local animal welfare committee.

Injectable ^{15}O-O_2 preparation

In the "injection" study, injectable ^{15}O-O_2 was used. Injectable ^{15}O-O_2 was prepared as described previously [10–12]. In brief, part of an infusion line kit (Terumo Corporation, Tokyo, Japan) and an artificial lung 18 cm in length (Senko Medical Instrument Mfg Co. Ltd., Tokyo, Japan) were connected using silicone tubing to make a closed system. Then, venous blood collected from a pig, which was used in the following PET studies, was added to the system and circulated (100 ml/min) by a peristaltic pump, followed by introduction of ^{15}O–O_2 gas (~7,000 MBq/min/433 ml) into the artificial lung for 15 min to prepare injectable ^{15}O-O_2 (5.6–60.7 MBq/ml).

In the "continuous infusion" study, the left femoral artery and right femoral vein were both cannulated. The two cannulas from the artery and the vein were connected to the opposite sides of an artificial lung to create a femoral shunt. The blood flow in the shunt was aided by a peristaltic pump (30–50 ml/min). ^{15}O-O_2 gas (~7,000 MBq/min/433 ml) was continuously introduced into the artificial lung.

PET protocol (Fig. 1)

The PET scanner was an ECAT EXACT HR (CTI/Siemens) [15], which has an imaging field of view (FOV) of 55 cm in diameter and 15 cm in axial length. The spatial resolution of the scanner is 5.8 mm in full width at half maximum at the center of the FOV.

After obtaining a 20-min transmission scan for attenuation correction and gas volume estimation, the blood pool image was obtained with a 4-min PET scan after the pigs inhaled 2.7 GBq ^{15}O-CO for 30 s. Arterial blood samples were taken every minute during the ^{15}O-CO scanning, and

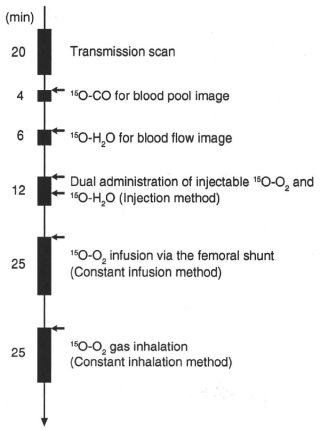

Fig. 1 Outline of the PET imaging study. The interval between scans was more than 15 min to allow for physical decay of O-15 radioactivity to background levels

the radioactivity concentration in the whole blood was measured with a NaI well-type scintillation counter calibrated against the PET scanner. Subsequently, ^{15}O-water was injected into the right femoral vein for 30 s at an infusion rate of 10 ml/min (injected radioactivity was about 1.11 GBq). Immediately after injection of ^{15}O-water, 26 dynamic frames (12×5 s, 8×15 s and 6×30 s) of PET data were acquired for 6 min.

Furthermore, two PET scans were successively performed after the IV injection of ^{15}O-O_2 (5.6–60.7 MBq/ml) for 30 s at an injection rate of 20–80 ml/min for the "injection" study, and by the continuous ^{15}O-O_2 gas infusion through the artificial lung in the femoral shunt for the "continuous infusion" study. In the "injection" study, 52 dynamic frames (12×5 s, 8×15 s, 6×30 s, 12×5 s, 8×15 s and 6×30 s) of PET data were acquired for 12 min, and 1.11 GBq of ^{15}O-water was injected IV for 30 s at 10 ml/min starting at 6 min after the administration of IV ^{15}O-O_2 according to the dual administration protocol we developed previously [16]. In the "continuous infusion" study, 26 dynamic frames (10×30 s, 5×60 s, 1×600 s and 10×30 s) were acquired for 25 min, and the 600-s frame was used for steady-state analysis.

Another PET scan was performed by ^{15}O-O_2 gas inhalation in one of the four pigs in the same protocol as the "continuous infusion" study. This was the "continuous inhalation" study. The interval between scans was more

than 15 min to allow for physical decay of O-15 radioactivity to background levels. All acquisitions were obtained in the two-dimensional mode (septa extended).

Data analysis

A filtered back-projection algorithm with a 6-mm Gaussian filter was used for image reconstruction. The reconstructed images had a matrix size of 128 × 128 × 47 and a voxel size of 1.84 × 1.84 × 3.38 mm, and all image data sets were resliced into short-axis images across the left ventricle [13].

Myocardial blood flow

rMBF was calculated from the injection of ^{15}O-H_2O by fitting the myocardial and arterial time-activity curve data to a single-tissue-compartment model that implemented corrections for partial-volume effects by introducing the tissue fraction. In addition, the model was corrected for spillover from the left ventricular (LV) chamber into the myocardial ROI by introducing the arterial blood volume [13]. In these experiments, the time-activity curves generated from large ROIs placed in the LV chamber were used as the input function.

Regional oxygen extraction fraction

In the "injection" study, rOEF was calculated according to Eqs. (2) and (5). In these formulations, F_{vein} was assumed to be 0.10 ml/g tissue and p was fixed at 0.90 ml/g. The blood volume image obtained from the ^{15}O-CO scan was used for the determination of V_B^{myo}. The value of $A_t(t)$ was obtained from the LV radioactivity concentration measured from the PET data set with small LV ROIs to minimize spillover from the myocardium. The calculation for the estimation of recirculating ^{15}O-H_2O was performed as previously described [16]. For the "continuous infusion" and "continuous inhalation" studies, in which a 600-s frame was regarded as steady-state, Eqs. (3) and (5) or Eqs. (3) and (4) were used for calculating rOEF, respectively.

Results

Table 1 summarizes the conditions of animals during the PET studies. The parameters were all within the physiologic range.

Figure 2 demonstrates the dynamic images obtained in the "injection", "continuous infusion", and "continuous inhalation" studies. With the injection and continuous-infusion methods, the right ventricle on the left side and the vena cava on the lower side were well delineated, whereas the left ventricle was moderately shown on the right side. The 16th frame (600~1,200 s after the initiation), which was used for steady-state analysis with the continuous-infusion method, was visibly distinct compared with all of the frames obtained with the injection method. However, with the continuous-inhalation method, neither ventricle could be depicted because of high radioactivity in the lung on the right and lower-side images.

The radioactivity in the blood pool obtained by ^{15}O-CO PET (Fig. 3g) and the gaseous volume estimated by inverse transmission data (Fig. 3h) were subtracted from the raw PET images (16th frame) with the continuous-inhalation and continuous-infusion methods, respectively (Fig. 3c and f). Both methods clearly delineated the myocardium after subtraction in comparison to the blood flow image (Fig. 3i). However, the continuous-inhalation method showed salient radioactivity on the lateral wall (Fig. 3c), whereas the continuous-infusion method showed only modest radioactivity in the myocardium (Fig. 3f). It is also notable that there was considerable radioactivity in the right ventricle with the continuous-infusion method even after the subtraction (Fig. 3f).

To further examine the differences between the continuous-infusion and continuous-inhalation methods, time-radioactivity curves during the PET scans were taken from four ROIs: the left ventricle (LV), right ventricle (RV), myocardium (Myo), and lung (Fig. 4). At the steady-state frame (600~1,200 s), the continuous-infusion method showed higher radioactivity in the RV and LV than in the myocardium (Fig. 4a), whereas the radioactivity of these regions was similar with the continuous-inhalation method (Fig. 4b). The radioactivity in LV was about two-thirds of that in RV in Fig. 4a, indicating that measurable radioactivity was excreted through the lung even after the femoral administration of ^{15}O-O_2. The lung excretion was also observed on the blood-subtracted image (Fig. 3e). Actually, there was significant radioactivity in the lung (Fig. 4a), although that was the lowest among the four ROIs. In contrast, the radioactivity in the myocardium was the lowest among the four ROIs with the continuous-inhalation method

Table 1 Physiological parameters of pigs during the PET studies

	pH	pCO_2 (mmHg)	pO_2 (mmHg)	tHb (g/dl)	O_2Sat (%)	HR (bpm)	BP (mmHg)	
							Diastolic	Systolic
Average	7.46	40.3	125.8	12.8	97.7	85	97.8	125.2
SD	0.032	2.51	16.69	1.30	1.83	19.5	10.4	19.3

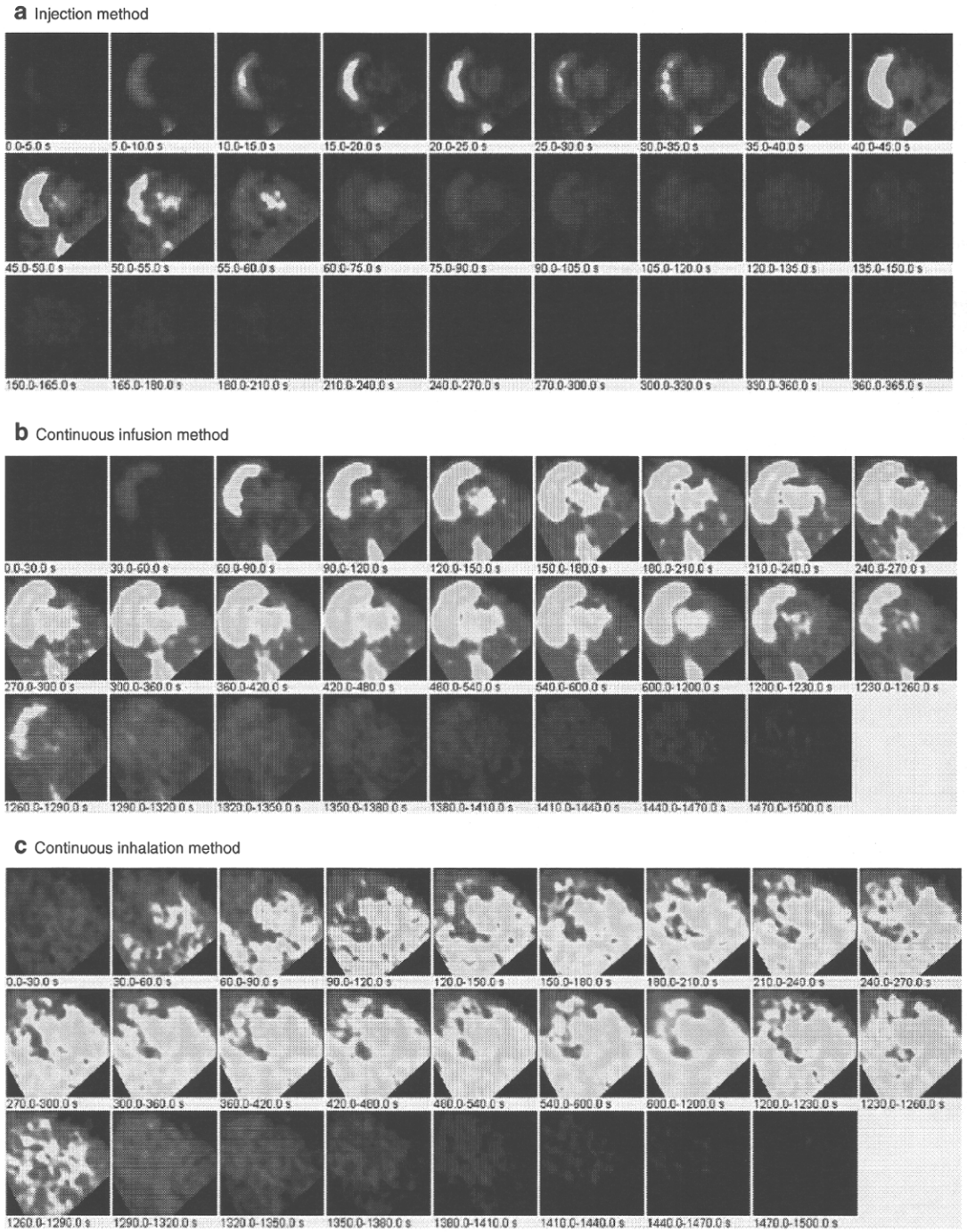

Fig. 2 PET images obtained in (**a**) the injection method, (**b**) the continuous-infusion method with injectable ^{15}O-O_2, and (**c**) the continuous-inhalation method with ^{15}O-O_2 gas

(Fig. 4b). The heart-to-lung radioactivity ratios were calculated from Fig. 4 for the quantitative estimation of image quality; the continuous-infusion method provided a ratio of 1.38±0.24, whereas the ratio was less than one with the continuous-inhalation method.

Table 2 shows the quantitative OEF values in the lateral wall obtained by the injection, continuous-infusion, and continuous-inhalation methods. These OEF values were consistent among the three methods.

Figure 5 represents the noise equivalent counts (NEC) standardized by the total counts detected by the PET scanner. Although the injection method tended to show rather high values, there was no significant difference between the values obtained by the injection and

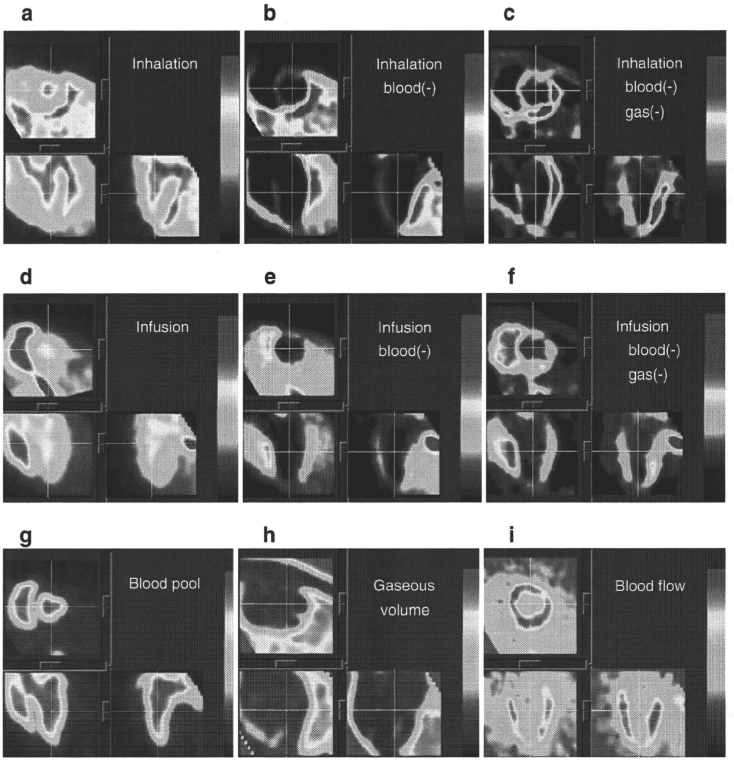

Fig. 3 PET images obtained in the study are shown. The 16th frame (steady-state frames) of the continuous-inhalation method and the continuous-infusion method are shown in (**a**) and (**d**), respectively. The 'blood-subtracted' images shown in (**b**) and (**e**) were created by subtraction of the blood-pool image by ^{15}O-CO (**g**) from (**a**) and (**d**). The 'blood- and gas-subtracted' images shown in (**c**) and (**f**) were created by the successive subtraction of the gaseous image (**h**) from (**b**) and (**e**). The myocardial blood flow image is also shown in (**i**)

continuous-infusion methods as determined by a Mann Whitney *U*-test.

Discussion

In previous studies, we showed the usefulness of the injectable ^{15}O-O_2 system for estimating cerebral oxygen metabolism in small animals such as rats under normal or ischemic conditions [10–12]. Injectable ^{15}O-O_2 replaced the inhalation protocol and radioactive ^{15}O-O_2 was administered via the tail vein. Thus, injectable ^{15}O-O_2 could abolish the artifact from the high radioactivity in the inhalation tube that distorts the PET images, especially in small animals. We considered that the concept could also be utilized in the hearts of large animals. Therefore, in the present study, we tested the feasibility of an injectable ^{15}O-O_2 system for estimating myocardial oxygen metabolism in normal pigs. In addition, since a shunt between the femoral artery and vein can be created in pigs but not in small animals, continuous infusion via the femoral shunt was also performed to achieve a constant and reliable delivery of radioactivity to the heart.

Dynamic PET scans showed a large difference in the radioactivity distribution among the three methods. Since the labeling efficiency to prepare injectable ^{15}O-O_2 was

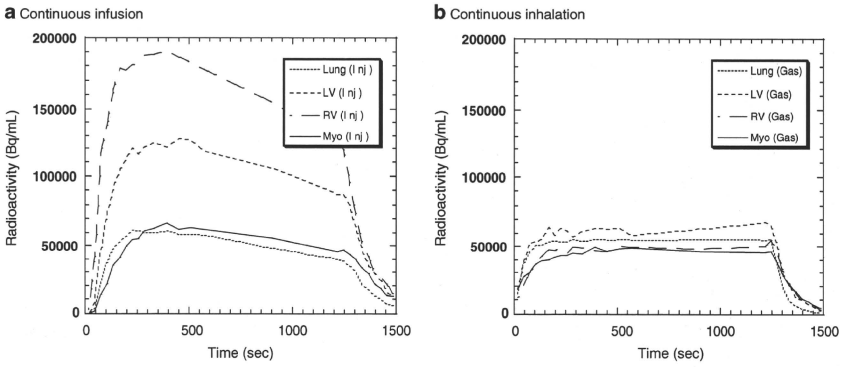

Fig. 4 Time-activity curves from the left ventricle (*LV*), the right ventricle (*RV*), the myocardium (lateral wall, Myo) and a lung region with the continuous-infusion method (**a**) and the continuous-inhalation method (**b**). The supply of radioactivity was started at time 0 s and stopped at 1,200 s. The 16th frame for the steady-state analysis was 600–1,200 s

lower with pig blood (ca. 61 MBq/ml at most) than with the blood of rats and humans (130 MBq/ml), the injection method provided rather obscure images. With the injection and continuous-infusion methods, the radioactivity in the lung was dramatically reduced in comparison to the continuous-inhalation method, since the heart-to-lung ratio with the continuous-infusion method was about 40% higher than with the continuous-inhalation method. This finding suggested that the two methods that inject radioactivity via a vein are more useful for analyzing myocardial oxygen metabolism in pigs than the continuous-inhalation method. However, a distinct difference between radioactivity of the right and left ventricles was observed in the images and time-radioactivity curves after venous administration of $^{15}O\text{-}O_2$, indicating a certain degree of excretion of the radioactivity by the lung. Therefore, the spillover from the pulmonary alveoli to the myocardium could not be omitted in the two methods with venous administration, and Eq. (4) was used for the OEF analysis, although the radioactivity in the lung was lower than that in the myocardium.

On the other hand, with the continuous-inhalation method, the radioactivity of the lung was in between the radioactivity in the RV and LV. This is curious because O-15 radioactivity was supplied from the inhalation tube and transferred from the lung to blood so that the radioactivity in the lung should have been the highest among the four ROIs. This may have been caused, in part, by inhomogeneous distribution of the radioactivity in the lung due to its structure in comparison with the myocardium and ventricles, and/or by artifacts from the lung to other

Table 2 OEF estimated by the three methods using injectable $^{15}O\text{-}O_2$ or $^{15}O\text{-}O_2$ gas

	OEF		
	Injection	Infusion	Inhalation
Pig. 1	0.70	0.72	
Pig. 2	0.67	0.72	
Pig. 3	0.71	0.74	
Pig. 4	0.76	0.69	0.72
Average	0.71	0.72	0.72
SD	0.036	0.020	

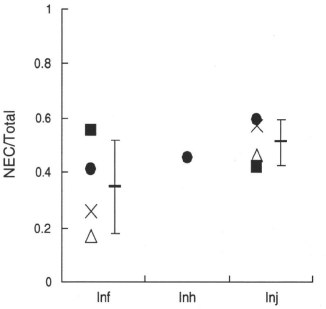

Fig. 5 The ratio of noise equivalent counts (*NEC*) to total counts in the total field of view of the PET scanner obtained with the continuous-infusion method (*Inf*), the continuous-inhalation method (*Inh*) and the injection method (*Inj*)

tissues. In any case, it is notable that the radioactivity in the myocardium was the lowest with the continuous-inhalation method, leading to difficulty in analyzing myocardial oxygen metabolism.

The OEF values in lateral walls were calculated to compare the ability of the three methods to determine myocardial oxygen metabolism by using the blood flow derived from the dual-administration protocol with the injection method and the single-administration protocol with the two continuous methods. There was no difference in the blood flow between the two protocols. Consequently, the three methods provided the same OEF value of about 0.7 and this is a physiological value in normal pigs, as was previously demonstrated [17, 18]. We have demonstrated the potential of the injectable ^{15}O-O_2 system for the estimation of physiological cerebral oxygen metabolism in rats and monkeys during early and late ischemia, hypertension, and ischemia plus hypertension [10–12, 19]. Therefore, we believe that the injection and continuous-infusion methods provide a physiological OEF in the myocardium. Nevertheless, we recognize the necessity to evaluate the reliability and usefulness of the injectable ^{15}O-O_2 method in myocardial applications. Further studies using pathophysiological animal models are required in the future, such as myocardial ischemia, hypoxia, and heart failure. On the other hand, since $MMRO_2$ is basically regarded as the product of MBF and OEF, the results indicated that these three methods were equivalent in their ability to quantify $MMRO_2$ in normal pigs, at least in the lateral wall. Although the images after the subtraction of spillovers from blood and gas showed different contrast between the continuous-infusion and continuous-inhalation methods, the ability of these two methods to measure OEF and $MMRO_2$ in the lateral walls was equivalent.

We did not evaluate myocardial oxygen metabolism in other heart regions since the radioactivity in the right ventricle could not be removed due to a significant difference of radioactivity between the ventricles with the continuous-infusion method. The injection method might be able to evaluate oxygen metabolism in other regions besides the lateral wall, although this was not evaluated in this study due to the low radioactivity of injectable ^{15}O-O_2 as described above. In the injection method, O-15 radioactivity was delivered from the femoral vein to RV, the lung, LV, and finally the myocardium. Thus, when the LV and myocardial activity reach a maximum, the RV activity is expected to be low. The later frames of the dynamic PET images with the injection method might avoid the high RV activity and delineate the myocardium and LV more clearly. With accurate anatomical information by gated PET/CT, the injection method will provide oxygen metabolism in other heart regions. In addition, the injection method has a benefit in that it is noninvasive and shortens the acquisition time in comparison with the continuous-infusion method. Future studies are needed to determine whether the injectable ^{15}O-O_2 system can be used in other heart regions.

With the injection method, the ratio of noise equivalent counts (NEC) to total counts tended to be the higher, probably because of the absence of high radioactivity adjacent to the PET scanner. Nevertheless, the continuous-infusion method did not show this tendency. This may be because tubes for the input to the artificial lung were positioned at the femoral shunt and the output to the drain of O-15 gas was positioned alongside the PET scanner, resulting in an increase of random counts during the study. Also, it is notable that the value with the continuous-inhalation method was not small, which suggests that the inhalation protocol itself did not worsen the results, but rather the high radioactivity in the lung might affect the analysis. In any case, if more care is given to shielding of the radioactivity in tubes and/or for arrangement of instruments in the PET room, a higher value of NEC/total counts will be obtained with the injectable ^{15}O-O_2 system.

The declining slope delineated in the time-activity curves with the continuous-infusion method requires some explanation. Since the flow rate of O-15 gas supply to the artificial lung positioned at the femoral shunt was maintained constant during the PET scan, it is possible that a decrease of labeling efficiency of the artificial lung occurred due to the deposition of any components of blood. The blood of rats or humans was negligibly deposited in the artificial lung during circulation at the same rate for at least 30 min in our other experiments, so that this problem may be specific for pigs. It is unclear which component in pig blood was exactly involved in the deposition and three of four pigs did not show a declining slope of the time-activity curve.

In practice, in routine studies on myocardial oxygen metabolism using large animals such as pigs, the continuous-inhalation method with ^{15}O-O_2 gas may be easier to perform for the following reasons: (1) the intubation tube used for gas anesthesia prior to the PET scan can also be used for ^{15}O-O_2 gas inhalation; (2) catheterization of the femoral artery and vein to create the femoral shunt for the continuous-infusion method may be troublesome; and (3) the injection of ^{15}O-O_2 requires an artificial lung, preparation time, and blood taken from the same animal prior to the PET scan. However, the injection of ^{15}O-O_2 has a substantial advantage over the continuous-inhalation method in that there is reduced radioactivity in the lung and clearer images of the heart are obtained. Therefore, the method for estimating myocardial oxygen metabolism should be selected depending on the objectives of the study and the surgical procedures. Furthermore, since radioactivity administered into the femoral vein is partially excreted into expired air, the injectable ^{15}O-O_2 system might be used for evaluating pulmonary function in the future.

Conclusion

In this study, we tested the feasibility of using an injectable ^{15}O-O_2 system to estimate myocardial oxygen metabolism in pigs. Both the bolus-injection and continuous-infusion methods reduced the radioactivity in the lung and provided similar OEF values in the lateral walls of the heart. These findings indicate that the injectable ^{15}O-O_2 system has the potential to evaluate myocardial oxygen metabolism.

References

1. Ohtake T. The review of myocardial positron emission computed tomography and positron imaging by gamma camera. Kaku Igaku. 1998;35:179–87.
2. Klein LJ, Visser FC, Knaapen P, Peters JH, Teule GJ, Visser CA, et al. Carbon-11 acetate as a tracer of myocardial oxygen consumption. Eur J Nucl Med. 2001;28:651–68.
3. Schelbert HR. PET contributions to understanding normal and abnormal cardiac perfusion and metabolism. Ann Biomed Eng. 2000;28:922–9.
4. Visser FC. Imaging of cardiac metabolism using radiolabelled glucose, fatty acids and acetate. Coron Artery Dis. 2001;12(Suppl 1):S12–8.
5. Hata T, Nohara R, Fujita M, Hosokawa R, Lee L, Kudo T, et al. Noninvasive assessment of myocardial viability by positron emission tomography with ^{11}C acetate in patients with old myocardial infarction. Usefulness of low-dose dobutamine infusion. Circulation. 1996;94:1834–41.
6. Yamamoto Y, de Silva R, Rhodes CG, Iida H, Lammertsma AA, Jones T, et al. Noninvasive quantification of regional myocardial metabolic rate of oxygen by $^{15}O_2$ inhalation and positron emission tomography. Experimental validation. Circulation. 1996;94:808–16.
7. Iida H, Rhodes CG, Araujo LI, Yamamoto Y, de Silva R, Maseri A, et al. Noninvasive quantification of regional myocardial metabolic rate for oxygen by use of $^{15}O_2$ inhalation and positron emission tomography. Theory, error analysis, and application in humans. Circulation. 1996;94:792–807.
8. Shidahara M, Watabe H, Kim KM, Oka H, Sago M, Hayashi T, et al. Evaluation of a commercial PET tomograph-based system for the quantitative assessment of rCBF, rOEF and $rCMRO_2$ by using sequential administration of ^{15}O-labeled compounds. Ann Nucl Med. 2002;16:317–27.
9. Mintun MA, Raichle ME, Martin WR, Herscovitch P. Brain oxygen utilization measured with O-15 radiotracers and positron emission tomography. J Nucl Med. 1984;25:177–87.
10. Magata Y, Temma T, Iida H, Ogawa M, Mukai T, Iida Y, et al. Development of injectable O-15 oxygen and estimation of rat OEF. J Cereb Blood Flow Metab. 2003;23:671–6.
11. Temma T, Magata Y, Kuge Y, Shimonaka S, Sano K, Katada Y, et al. Estimation of oxygen metabolism in a rat model of permanent ischemia using positron emission tomography with injectable ^{15}O-O_2. J Cereb Blood Flow Metab. 2006;26:1577–83.
12. Temma T, Kuge Y, Sano K, Kamihashi J, Obokata N, Kawashima H, et al. PET O-15 cerebral blood flow and metabolism after acute stroke in spontaneously hypertensive rats. Brain Res. 2008;1212:18–24.
13. Watabe H, Jino H, Kawachi N, Teramoto N, Hayashi T, Ohta Y, et al. Parametric imaging of myocardial blood flow with ^{15}O-water and PET using the basis function method. J Nucl Med. 2005;46:1219–24.
14. Iida H, Rhodes CG, de Silva R, Yamamoto Y, Araujo LI, Maseri A, et al. Myocardial tissue fraction–correction for partial volume effects and measure of tissue viability. J Nucl Med. 1991;32:2169–75.
15. Wienhard K, Dahlbom M, Eriksson L, Michel C, Bruckbauer T, Pietrzyk U, et al. The ECAT EXACT HR: performance of a new high resolution positron scanner. J Comput Assist Tomogr. 1994;18:110–8.
16. Kudomi N, Hayashi T, Teramoto N, Watabe H, Kawachi N, Ohta Y, et al. Rapid quantitative measurement of $CMRO_2$ and CBF by dual administration of ^{15}O-labeled oxygen and water during a single PET scan-a validation study and error analysis in anesthetized monkeys. J Cereb Blood Flow Metab. 2005;25:1209–24.
17. Alders DJ, Groeneveld AB, de Kanter FJ, van Beek JH. Myocardial O_2 consumption in porcine left ventricle is heterogeneously distributed in parallel to heterogeneous O_2 delivery. Am J Physiol Heart Circ Physiol. 2004;287:H1353–61.
18. Van Woerkens EC, Trouwborst A, Duncker DJ, Koning MM, Boomsma F, Verdouw PD. Catecholamines and regional hemodynamics during isovolemic hemodilution in anesthetized pigs. J Appl Physiol. 1992;72:760–9.
19. Temma T, Magata Y, Iida H, Hayashi T, Ogawa M, Mukai T, et al. Development of injectable O-15 oxygen and its application for estimation of OEF. International Congress Series, Quantitation in Biomedical Imaging with PET and MRI Proceedings of the International Workshop on Quantitation in Biomedical Imaging with PET and MRI. 2004;1265:262–65.